An Approach Using Highly Sensitive Carbon Nanotube Adhesive Films for Crack Growth Detection under Flexural Load in Composite Structures

Xoan F. Sánchez-Romate[a,b,], Rocío Moriche[b,c], Alberto Jiménez-Suárez[b], María Sánchez[b], Alfredo Güemes[a] and Alejandro Ureña[b]*

[a] Department of Aerospace Materials and Processes, Escuela Técnica Superior de Ingenieros Aeronáuticos, Universidad Politécnica de Madrid, Plaza del Cardenal Cisneros 3, 28040 Madrid, Spain

[b] Materials Science and Engineering Area, Escuela Superior de Ciencias Experimentales y Tecnología, Universidad Rey Juan Carlos, Calle Tulipán s/n, 28933 Móstoles (Madrid), Spain

[c] Departamento de Ingeniería y Ciencia de los Materiales y del Transporte, Universidad de Sevilla, Avda. Camino de los Descubrimientos, s/n, 41092 Sevilla, Spain

*Corresponding author: xoan.fernandez.sanchezromate@urjc.es Tel: +34914888252

ABSTRACT

Sensing capabilities of carbon nanotube (CNT) doped adhesive films under bending conditions were investigated. Standard Mode-II coupons and skin-stringer sub-elements were manufactured while their electrical resistance was monitored. Mode-II energy fracture was improved when adding CNTs in comparison to neat adhesive joints due to their toughening effect. Electrical monitoring showed a stable increase of the electrical resistance with crack length with lower sensitivity than Mode-I testing due to a lower crack opening effect. A good agreement was observed by comparing to theoretical estimations, indicating a uniform adhesive distribution inside the joint, confirmed by SEM analysis. Monitoring tests on skin-stringer sub-elements subjected to bending load showed a similar behavior but some sharp increases were observed, especially in the last stages of the test, due to a less uniform adhesive distribution in the central region. Therefore, the proposed technique shows a high potential and applicability for Structural Health Monitoring of composite structures.

Keywords: carbon fiber structures; adhesives; carbon nanotubes; SHM; mechanical properties

1. INTRODUCTION

Carbon Fiber Reinforced Polymer (CFRP) materials are now of interest because of their high specific as well as some physical properties such as a good corrosion resistance in comparison to conventional metallic alloys. Therefore, the increasing complexity of composite structures has promoted the development of proper assembly techniques.

In this regard, bonded joints present some advantages over bolted connections such as a weight saving and the absence of stress concentrators around the bolt holes *(1)* but their reliability is not totally ensured by the available inspection techniques. They are mainly based in Fiber Bragg Gratings (FBGs), Ultrasonic Waves or Acoustic Emission systems *(2-6)*. However, their main limitation is that they do not often give a global and complete information about the damage and the obtained signal is sometimes very difficult to analyze and requires complex numerical techniques *(7-10)*. In addition to that, the identification of debonding in adhesive joints is especially difficult and these techniques sometimes do not give a very accurate information about this issue *(6, 10)*.

In this context, carbon nanotubes (CNTs), since the first studies by S. Iijima,*(11)* have demonstrated a huge potential as they have excellent mechanical and electrical properties *(12-15)*, being suitable for SHM applications by electrical resistance monitoring *(16-22)*.

The CNT capability for SHM applications is based on their piezoresistivity and the tunneling effect between adjacent nanoparticles *(23-26)*, leading to higher gauge factors, defined as the change of the normalized electrical resistance divided by the applied strain, than conventional metallic foils *(27, 28)*. For these reasons they are able to properly identify and quantify some defects such as delaminations or cracks *(29, 30)*.

In previous studies, the effect of CNTs on bonded joints has been investigated by using novel adhesive films sprayed with an aqueous CNT solution *(31, 32)*. This CNT dispersion is done by means of ultrasonication and helped by the addition of a surfactant Sodium-Dodecyl-Sulfate (SDS). Sensing capabilities of CNT doped adhesive films have been demonstrated in Single Lap Shear (SLS) and Mode-I tests. In fact, it has been possible to distinguish between different failure and crack propagation modes by analyzing the electrical response, showing a good agreement and high sensitivity *(33)*.

In this regard, this study aims to analyze the crack propagation under bending conditions on adhesive joints by using the proposed CNT doped adhesive film and their capability for SHM of more complex structures. For that purpose, Mode-II standard specimens and stiffened elements were tested in similar load conditions. The main goal is to get a deeper knowledge about sensing capabilities of CNT doped adhesive films and prove their potential for crack detection in simple sub-elements subjected to more complex load states. Moreover, the comparison between the standard coupons and the sub-elements will give a more complete overview of SHM capabilities of the proposed adhesive films.

In addition to that fact, a simple theoretical model has been proposed to correlate the electrical signal and the mechanical performance of the joints, similar to previous theoretical estimations *(33)*, showing the differences between Mode-I and Mode-II crack propagation. Furthermore, a microstructural characterization of the transversal section and fracture surfaces has been carried out in order to know the adhesive distribution along the joint and identify possible manufacturing defects.

2. EXPERIMENTAL PROCEDURE

2.1 Adhesive preparation

The adhesive used for this study was a *FM 300K*, supplied by *Cytec*. It is an epoxy-based adhesive film with a knit tricot carrier typical in aerospace applications for joining CFRP-CFRP and CFRP-metal substrates.

Multi-wall carbon nanotubes (MWCNTs) are supplied by *Nanocyl* with a commercial name *NC7000*. They have an average diameter of 10 nm and a length up to 1.5 μm.

The addition of the CNTs to the adhesive film is done by spraying an aqueous CNT dispersion over the adhesive surface at 1 bar. The dispersion is achieved by means of

ultrasonication during 20 min, with the help of a surfactant called sodium-dodecyl-sulfate (SDS). CNT and SDS content are fixed at 0.1 and 0.25 wt. %. After that, water is removed by drying the adhesive at 70 ºC during 30 min. All of these parameters are set based on a previous study *(32)*.

2.2 Manufacturing of normalized coupons and stiffened elements

Normalized bonded joints are manufactured by secondary bonding in a uniaxial hot press. CFRP substrates are Unidirectional (UD) laminates of 150 × 25 × 3.5 mm^3 with a peel-ply surface treatment. Cure cycle conditions are described in Table 1. A Teflon of 40 mm is placed at the beginning of the joint to induce the pre-crack for Mode-II testing.

Stiffened elements are manufactured by secondary bonding of a flat skin of 150 × 300 mm^2 with a layer sequence $[\pm 45/90/]_S$ and a T-stringer using a vacuum bag as shown in Figure 1. The curing temperature was set as previously described in Table 1. Secondary bonding is set as the manufacturing technique to directly compare the monitoring tests of the stiffened elements with those obtained from normalized coupons. The pre-crack is made by placing a Teflon insert of 16 mm at the beginning (25 % of the width of the stringer, similar to Mode-II standard coupons, highlighted in red in Figure 1).

2.3 Electromechanical and microstructural characterization

Monitoring of both normalized coupons and skin-stringer sub-elements was carried out by means of electrical resistance measurement using a hardware *Agilent 34401A*.

Electrodes were placed as shown in the schematics of Figure 2 and were made of copper wire sealed to the CFRP substrate with silver ink and protected from the environment with an adhesive layer.

Mechanical tests were conducted at a test rate of 1 mm/min in both coupons and sub-elements. In the case of standard coupons, four tests were conducted for each neat and CNT-doped adhesive conditions. Two skin-stringer sub-elements were tested with the CNT-doped adhesive film. One representative example of each condition is shown in the Results and Discussion section.

Microstructural analysis of the transversal sections of normalized coupons and skin-stringer sub-elements was carried out by Scanning Electron Microscopy (SEM) using a *S-3400 N* apparatus from *Hitachi*. The samples were coated by a thin layer of gold and SEM images were taken at different magnifications for a better characterization.

3. RESULTS AND DISCUSSION

This section shows the main results of the electromechanical tests of the CNT doped adhesive joints under bending conditions. Firstly, the mechanical behavior of the Mode-II adhesive joints is analyzed by comparing the fracture energy values of doped and non-doped bonded joints. Simultaneously, the electrical response of the standard Mode-II coupons is also analyzed and compared to the crack propagation through the joint. Then, the most representative results of the sub-elements under bending loading are shown and a comparison with the Mode-II specimen is carried out. Simultaneously, a microstructural study of the bonding line and the fracture surfaces is given.

3.1 Mode-II mechanical behavior

By using the Timoshenko beam theory for End Notched Flexure (ENF) test, the specimen compliance ($C = \delta/P$, being δ and P the displacement and the load, respectively) is written as follows:

$$C = \frac{3a^3 + 2L^3}{8E_1Bh^3} + \frac{3L}{10G_{13}Bh} \quad (1)$$

Where a is the crack length, L the half length of the span, B and h the width and the thickness of the substrate and $E_1$and G_{13} its longitudinal and shear moduli, respectively,

Therefore, it is possible to calculate the equivalent crack length, a_e from the current specimen compliance by rewriting the Equation (1):

$$a_e = \left(\frac{1}{3}\left(\left(C - \frac{3L}{10G_{13}Bh}\right)8E_1Bh^3 - 2L^3\right)\right)^{\frac{1}{3}} \quad (2)$$

The strain energy release rate under mode II can be calculated by using the Irvin-Kies equation:

$$G_{II} = \frac{P^2 dC}{2Bda} \quad (3)$$

Combining the Equations (2) and (3) it is possible to obtain the G_{II} value:

$$G_{II} = \frac{9P^2{a_e}^2}{16B^2h^3E_1} \quad (4)$$

Figure 3 shows the mechanical curves of the CNT-doped and neat adhesive joints. Both neat and CNT-doped joints show an expected behavior, in according to other studies *(34, 35)*. The peak load of the force-displacement curve (Figure 3(a)) is slightly higher in the case of CNT-doped bonded joints. By analyzing the $G_{II} - a_e$ curves (also called R-curves) some differences can be observed when adding CNTs to the adhesive film (Figure 3(b)). A slower crack propagation is observed in the CNT-doped sample, leading, thus to a higher value of the fracture energy, around 5 N/mm, in comparison to the neat joints (4.2 N/mm). This enhancement is explained by a good CNT homogeneity, with the absence of larger agglomerates which can induce an embrittlement *(32, 36)*. These results are in good agreement with those observed in Mode-I crack propagation testing *(33)* and can be

explained because of the bridging and toughening effect of CNTs, making the crack propagation along the joint harder *(37-39)*.

Therefore, the CNT addition enhances the fracture energy and leads to a slower crack propagation. As a further step, the huge increase of the electrical conductivity induced by the CNT percolating networks will be used as a method for on-line crack growth monitoring.

3.2 Mode-II electromechanical analysis

Figure 4 shows an example of the electromechanical behavior of Mode-II standard specimens. By observing the graph of Figure 4(a), it is noticed that there is a sudden increase of the electrical resistance corresponding to the first drop on the mechanical response. This is correlated with the initial crack propagation through the bonded joint in a similar way than previously observed for Mode-I specimens in other studies *(33)*. Then, there is an increase of the electrical resistance until final failure of the specimen due to a continuous breakage of electrical pathways.

It is important to notice that there is an initial increase of the electrical resistance before crack starts to propagate. This initial increase is associated to the bending effect of the specimens, which induces the adhesive deformation, leading to an increase on the tunneling distance between adjacent CNTs and thus, to an electrical resistance growth. After that, a steady increase of the electrical resistance is observed.

By analyzing the crack propagation and the electrical response, shown in Figure 4 (b) it is observed that there is a very good agreement between the crack length and the corresponding measured electrical resistance. It is observed that a faster crack propagation is directly correlated to a higher increase of the electrical resistance as there is a sudden breakage of the electrically conductive pathways.

Figure 5 shows the electrical resistance change as a function of the crack length and crack propagation velocity. The crack propagation velocity is calculated from crack length measurements following this formula:

$$v = \frac{\Delta a}{\Delta t} \tag{5}$$

Where Δa is the crack length change during a known time interval Δt.

It is noticed that the increase of the electrical resistance as a function of the crack length is smooth, although some slight sharp increases are also observed (highlighted in the graph as points 1 and 2). These sudden changes are correlated to areas with higher crack propagation velocity and with a sudden drop in the load. This faster crack propagation can be correlated to an irregular crack growth, in a similar way than the stick-slip effect shown in Mode-I testing.

In order to have a deeper knowledge of the electromechanical behavior of the adhesive joints, it is possible to make a first estimation of the electrical response as a function of the crack length. For this purpose, a similar theoretical model than the developed for Mode-I specimens *(33)* is proposed, given by the following expression valid for an ideal adhesive joint:

$$\frac{\Delta R}{R_0} = \frac{A_0}{A} - 1 = \frac{b \cdot L}{b \cdot (L - a)} - 1 \tag{6}$$

Where *b* and *L* are the width and the total length of the adhesive joint.

Figure 6 presents the theoretical predictions versus experimental measurements of the electrical resistance. The electrical behavior is found to be similar as there is a steady increase of the electrical resistance. However, the sensitivity, defined as the change of the normalized resistance divided by the crack length, is quite different (Figure 6 (a)). It is noticed that the theoretical sensitivity is higher than the experimental one. This can be explained because of the differences between Mode-I and Mode-II crack propagation. In

the first case, the crack opening is much more relevant as each substrate moves in an opposite direction (Figure 7). However, in the case of Mode-II this effect is less significant as both substrates move in a parallel plane. In addition, there is a relative displacement of the substrate in an opposite way due to the bending effect *(34)*. This implies a lower sensitivity as there is a higher proximity between conductive pathways than in Mode-I crack opening (Figure 7). For these reasons, it is necessary to apply a corrective factor, *K*, taking the lower crack opening effect into account. In this case, the Equation (6) will be rewritten as follows:

$$\frac{\Delta R}{R_0} = K \cdot \left(\frac{b \cdot L}{b \cdot (L - a)} - 1 \right) \tag{7}$$

The value of *K* can give a first estimation of this crack opening effect. A value below 1 indicates that the crack is not totally open such as in Mode-I testing. Therefore, after applying the expression of Equation (7) with a *K* coefficient of 0.33, a good agreement with experimental results is observed, as noticed in the dashed line of Figure 6 (b). This means that there is no a high opening effect of the crack during the test, and that the adhesive joint does not present significant manufacturing defects such as porosity or thickness variation. Therefore, CNT adhesive distribution can be considered homogeneous along the bonded joint, without sharp increases in the electrical resistance *(33)*. This statement can be confirmed by an analysis of the transversal section and fracture surfaces.

Figure 8 shows an image of the fracture surface of the bonded joint. The failure mode is mainly cohesive and the adhesive distribution is similar in both substrates. In addition, a uniform adhesive distribution is observed in the fracture surface along the bonded joint showing no darker bands, in an opposite way than the previously observed results for Mode-I testing *(33)*. This is in good agreement with the electromechanical results,

showing a soft crack propagation in contrast to stick-slip behavior where the fracture surfaces usually present a stick-slip pattern *(33, 40)*.

Microstructural characterization reveals a reasonable uniform thickness distribution, ranging from 200-250 μm (Figures 9 (a) and (b)). Some voids are observed along the joint. Their presence can be explained by the curing conditions. A uniaxial pressure is applied by using a hot press, inducing an adhesive overflow to the edges and causing a lack of adhesive in several parts of the joint. This can be solved by applying a uniform pressure in every direction, for example by using an autoclave.

In addition to that fact, it is noticed that the interface between the substrate and the adhesive shows a good continuity, leading to a high quality of the interface (Figure 9 (c)). A globular distribution of the adhesive is observed in the interface due to the peel-ply surface treatment (Figure 9 (d)), which induces a controlled roughness.

Therefore, the proposed method has proved its applicability for crack propagation monitoring under bending conditions in standard coupons. Thus, in order to further investigate the adhesive monitoring capabilities under bending loading, the electromechanical response of skin-stringer sub-elements is going to be analyzed.

3.3 Skin-stringer bending analysis

Figure 10 shows an example of the electromechanical response of the skin-stringer sub-element when subjected to flexure load. In a similar way to mode-II normalized coupon test, the electrical resistance increases with crack propagation due to the breakage of the electrical pathways. It is observed that when the crack reaches the middle point of the stringer, that is, 17 mm, (Figure 10 (b)) the variation of electrical resistance is about 20 %, showing a similar sensitivity than in the coupon tests. This is also explained by the way in which electrical pathways are breaking during the test.

The electrical resistance of the specimen, supposing that the conductivity of the CFRP substrates is much higher than the adhesive and, thus, this contribution to the electrical resistance can be negligible, can be defined by the following expression:

$$\Delta R = \Delta R_{crack} + \Delta R_{bending} \quad (8)$$

Where ΔR is the variation of total resistance of the specimen and ΔR_{crack} and $\Delta R_{bending}$ the resistance change due to the crack propagation and the bending effect, respectively.

The mechanical behavior of the specimen is described in the schematics of Figure 11. The region where crack propagates shows a similar behavior than in Mode-I testing with a crack opening. Therefore, the contribution due to ΔR_{crack} is higher than in the case of normalized coupons, that is $\Delta R_{crack_{stiffned}} > \Delta R_{crack_{coupon}}$. On the other hand, there is more prevalent compressive effects in the adhesive layer when looking the region where there is no crack propagation due to the higher thickness of the stiffened element. This compression effects leads to a reduction in the tunneling distance between adjacent nanoparticles leading to a reduction of $R_{bending}$ in comparison to mode-II tests where the adhesive layer is placed near the neutral axis and, thus, the variation of $R_{bending}$ is approximately zero, that is, $R_{bending_{stiffened}} < R_{bending_{coupon}}$. Therefore, the variation of the electrical resistance, $\Delta R_{stiffned}$, during the bending tests, when applying Equation (8) is similar to mode-II normalized tests, ΔR_{coupon}.

Moreover, Figure 12 shows the variation of the electrical and mechanical response as a function of the crack length and crack propagation velocity. There are slight differences that can be attributed to a more complex strain distribution in the skin-stringer element than in the mode-II normalized coupons, requiring a deeper theoretical analysis. However, it can be noticed that there is a good agreement between the expected electrical response, calculated by using the expression of Equation (7) (dash lines), with the same

correction factor K=0.33, and the measured one during the test. Some differences are found in the last stages of the bending test, probably due to a more irregular adhesive distribution inside the joint. Therefore, the proposed method shows a good applicability also in more complex elements such as stiffened panels.

The analysis of fracture surfaces (Figure 13) of the skin-stringer sub-elements reveals a good uniformity of the adhesive distribution and a mainly cohesive failure, in a similar way to the previously described normalized coupons, justifying again the softer evolution of the electrical resistance in comparison to mode-I tests.

Figure 14 shows several SEM images of the transversal section of the T and web regions. The peel-ply treatment of the stringer face results in a better interface than in the skin side, treated by brushing, where crack trends to propagate preferentially (Figure 14 (a)). The typical globular distribution of the adhesive due to the peel-ply roughness is also observed in a similar way than to mode-II coupons. In this case, the thickness distribution of the adhesive joint is not as uniform as at coupon level due to the stiffener effect. Therefore, a lower thickness is observed in the central area (around 130 μm, as observed in Figure 14 (b)) in comparison to the web region around 190 μm, as observed in Figure 14 (c)) where the effect of the stiffener weight is not as prevalent. This would explain the sharper evolution of the electrical resistance in the last stages of the test due to a breakage of prevalent pathways in the central region of the stiffener. The crack opening is observed to be more significant in the web region (Figure 14 (d)). However, the crack end is narrow (Figure 14 (e)) and several crack-bridging is observed (Figure 14 (f)), which induces a not completely breakage of electrical pathways, leading to lower values of resistance and sensitivity, as commented before. In addition, some localized voids are observed inside the adhesive joint (Figures 14 (d) and (e)). In this case, these voids are identified as some porosity induced by the vacuum conditions during curing, leading to a lack of compaction.

4. CONCLUSIONS

Mode-II crack propagation monitoring capabilities of CNT doped adhesive films have been investigated at coupon and at sub-element level.

The electrical resistance increases with crack propagation as there is a breakage of electrical pathways. This variation differs from mode-I testing where the sensitivity is much higher, because of the effect of crack opening. In addition to that, the change of the electrical resistance does not show sharp increases and arrest phases due to a stable crack growth and a good adhesive homogeneity.

In addition, an enhancement of G_{IIC} is observed when comparing to non-doped adhesive joints due to the toughening effect of the carbon nanotubes, leading to a slower crack propagation.

Moreover, bending tests were also conducted in skin-stringer sub-elements. A similar electrical response has been observed. In this case, there is two opposite effects affecting the electrical behavior: the higher resistance changes due to crack opening and the compressive state due to bending loads.

Microstructural analysis reveals a good uniformity in the adhesive thickness distribution in case of standard coupons. Skin-stringer elements show a lower adhesive thickness in central region of the T-stringer, resulting in a more prevalent breakage of electrical pathways in the last stages of the tests. In addition, there are presence of voids due to adhesive overflow in normalized coupons and a general porosity due to a lack of compaction in the skin-stringer elements.

Therefore, the proposed technology has proved its potential and applicability for monitoring CFRP bonded joints subjected to bending conditions at coupon and sub-element level being a promising technique for SHM applications on composite structures.

ACKNOWLEDGEMENTS

This work was supported by the Ministerio de Economía y Competitividad of Spanish Government [PROJECT MAT2016-78825-C2-1-R] and Comunidad de Madrid regional government [PROJECT 2013/MIT-2862].

DATA STATEMENT

The raw/processed data required to reproduce these findings cannot be shared at this time due to technical or time limitations. It will be made available on request.

REFERENCES

1. Hussey R, Wilson J. Structural Adhesives: Directory and Databook. Springer Science & Business Media; 1996.

2. Palaniappan J, Ogin SL, Thorne AM, Reed GT, Crocombe AD, Capell TF, et al. Disbond growth detection in composite-composite single-lap joints using chirped FBG sensors. Composites Sci Technol. 2008 SEP 2008;68(12):2410-7.

3. Bernasconi A, Carboni M, Comolli L. Monitoring of fatigue crack growth in composite adhesively bonded joints using fiber Bragg gratings. Procedia Engineering. 2011;10:207-12.

4. Malinowski P, Wandowski T, Ostachowicz W. The use of electromechanical impedance conductance signatures for detection of weak adhesive bonds of carbon fibre–reinforced polymer. Structural Health Monitoring. 2015;14(4):332-44.

5. Sherafat MH, Guitel R, Quaegebeur N, Hubert P, Lessard L, Masson P. Structural health monitoring of a composite skin-stringer assembly using within-the-bond strategy of guided wave propagation. Mater Des. 2016 JAN 15 2016;90:787-94.

6. Tamborrino R, Palumbo D, Galietti U, Aversa P, Chiozzi S, Luprano VAM. Assessment of the effect of defects on mechanical properties of adhesive bonded joints by using non destructive methods. Composites Part B: Engineering. 2016 4/15;91:337-45.

7. Froggatt M, Moore J. High-spatial-resolution distributed strain measurement in optical fiber with Rayleigh scatter. Appl Opt. 1998;37(10):1735-40.

8. Basri R, Chiu W. Numerical analysis on the interaction of guided Lamb waves with a local elastic stiffness reduction in quasi-isotropic composite plate structures. Composite structures. 2004;66(1):87-99.

9. Palaniappan J, Wang H, Ogin SL, Thorne AM, Reed GT, Crocombe AD, et al. Changes in the reflected spectra of embedded chirped fibre Bragg gratings used to monitor disbonding in bonded composite joints. Composites Sci Technol. 2007 OCT 2007;67(13):2847-53.

10. Habib F, Martinez M, Artemev A, Brothers M. Structural health monitoring of bonded composite repairs - A critical comparison between ultrasonic Lamb wave approach and surface mounted crack sensor approach. Composites Part B-Engineering. 2013 APR 2013;47:26-34.

11. Iijima S. Helical Microtubules of Graphitic Carbon. Nature. 1991 NOV 7 1991;354(6348):56-8.

12. Ruoff RS, Lorents DC. Mechanical and thermal properties of carbon nanotubes. carbon. 1995;33(7):925-30.

13. Xie S, Li W, Pan Z, Chang B, Sun L. Mechanical and physical properties on carbon nanotube. Journal of Physics and Chemistry of solids. 2000;61(7):1153-8.

14. Popov VN. Carbon nanotubes: properties and application. Materials Science and Engineering: R: Reports. 2004;43(3):61-102.

15. Gan L, Dong M, Han Y, Xiao Y, Yang L, Huang J. Connection-improved conductive network of carbon nanotubes in the rubber crosslink network. ACS applied materials & interfaces. 2018.

16. Li C, Thostenson ET, Chou T. Sensors and actuators based on carbon nanotubes and their composites: A review. Composites Sci Technol. 2008 MAY;68(6):1227-49.

17. Hu N, Karube Y, Arai M, Watanabe T, Yan C, Li Y, et al. Investigation on sensitivity of a polymer/carbon nanotube composite strain sensor. Carbon. 2010 MAR 2010;48(3):680-7.

18. Gao L, Chou T, Thostenson ET, Zhang Z, Coulaud M. In situ sensing of impact damage in epoxy/glass fiber composites using percolating carbon nanotube networks. Carbon. 2011 AUG;49(10):3382-5.

19. Cao X, Wei X, Li G, Hu C, Dai K, Guo J, et al. Strain sensing behaviors of epoxy nanocomposites with carbon nanotubes under cyclic deformation. Polymer. 2017 MAR 10;112:1-9.

20. Datta S, Neerukatti RK, Chattopadhyay A. Buckypaper embedded self-sensing composite for real-time fatigue damage diagnosis and prognosis. Carbon. 2018;139:353-60.

21. Khashaba UA. Static and fatigue analysis of bolted/bonded joints modified with CNTs in CFRP composites under hot, cold and room temperatures. Composite Structures. 2018 15 June 2018;194:279-91.

22. Boztepe S, Liu H, Heider D, Thostenson ET. Novel carbon nanotube interlaminar film sensors for carbon fiber composites under uniaxial fatigue loading. Composite Structures. 2018 1 April 2018;189:340-8.

23. Alamusi, Hu N, Fukunaga H, Atobe S, Liu Y, Li J. Piezoresistive Strain Sensors Made from Carbon Nanotubes Based Polymer Nanocomposites. Sensors. 2011 NOV;11(11):10691-723.

24. Loyola BR, Zhao Y, Loh KJ, La Saponara V. The electrical response of carbon nanotube-based thin film sensors subjected to mechanical and environmental effects. Smart Mater Struct. 2013 FEB;22(2):025010.

25. Sanli A, Benchirouf A, Mueller C, Kanoun O. Piezoresistive performance characterization of strain sensitive multi-walled carbon nanotube-epoxy nanocomposites. Sensors and Actuators A-Physical. 2017 FEB 1;254:61-8.

26. Reddy SK, Kumar S, Varadarajan KM, Marpu PR, Gupta TK, Choosri M. Strain and damage-sensing performance of biocompatible smart CNT/UHMWPE nanocomposites. Materials Science and Engineering: C. 2018 1 November 2018;92:957-68.

27. Cao J, Wang Q, Dai H. Electromechanical properties of metallic, quasimetallic, and semiconducting carbon nanotubes under stretching. Phys Rev Lett. 2003 APR 18;90(15):157601.

28. Cullinan MA, Culpepper ML. Carbon nanotubes as piezoresistive microelectromechanical sensors: Theory and experiment. Physical Review B. 2010 SEP 16;82(11):115428.

29. Loyola BR, La Saponara V, Loh KJ, Briggs TM, O'Bryan G, Skinner JL. Spatial Sensing Using Electrical Impedance Tomography. Ieee Sensors Journal. 2013 JUN;13(6):2357-67.

30. Tallman TN, Gungor S, Wang KW, Bakis CE. Tactile imaging and distributed strain sensing in highly flexible carbon nanofiber/polyurethane nanocomposites. Carbon. 2015 DEC;95:485-93.

31. Garcia C, Sanchez M, Urena A, Rams J. Carbon Nanotubes for Assessing the Structural Integrity of Composite Bonded Joints with Film Adhesives. Structural Health Monitoring 2015: System Reliability for Verification and Implementation, Vols.1 and 2. 2015 2015:2169-76.

32. Sánchez-Romate XF, Jiménez-Suárez A, Molinero J, Sánchez M, Güemes A, Ureña A. Development of bonded joints using novel CNT doped adhesive films: Mechanical and electrical properties. International Journal of Adhesion and Adhesives. 2018 November 2018;86:98-104.

33. Fernández Sánchez-Romate XX, Molinero J, Jiménez-Suárez A, Sánchez M, Güemes A, Ureña A. Carbon Nanotube Doped Adhesive Films for Detecting Crack Propagation on Bonded Joints: A Deeper Understanding of Anomalous Behaviors. ACS applied materials & interfaces. 2017.

34. Fernandes RMRP, Chousal JAG, de Moura MFSF, Xavier J. Determination of cohesive laws of composite bonded joints under mode II loading. Composites Part B-Engineering. 2013 SEP;52:269-74.

35. Fernandes RL, de Moura MFSF, Moreira RDF. Effect of moisture on pure mode I and II fracture behaviour of composite bonded joints. International Journal of Adhesion and Adhesives. 2016 July 2016;68:30-8.

36. Burkholder GL, Kwon YW, Pollak RD. Effect of carbon nanotube reinforcement on fracture strength of composite adhesive joints. J Mater Sci. 2011 MAY;46(10):3370-7.

37. Hsieh TH, Kinloch AJ, Taylor AC, Kinloch IA. The effect of carbon nanotubes on the fracture toughness and fatigue performance of a thermosetting epoxy polymer. J Mater Sci. 2011 DEC;46(23):7525-35.

38. Gude MR, Prolongo SG, Urena A. Toughening effect of carbon nanotubes and carbon nanofibres in epoxy adhesives for joining carbon fibre laminates. Int J Adhes Adhes. 2015 OCT;62:139-45.

39. Li X, Zhang W, Zhai S, Tang S, Zhou X, Yu D, et al. Investigation into the toughening mechanism of epoxy reinforced with multi-wall carbon nanotubes. E-Polymers. 2015 SEP;15(5):335-43.

40. Ashcroft IA, Hughes DJ, Shaw SJ. Mode I fracture of epoxy bonded composite joints: 1. Quasi-static loading. Int J Adhes Adhes. 2001 APR 2001;21(2):87-99.

FIGURE CAPTIONS

Figure 1: Image of the vacuum bag used in the manufacturing of skin-stringer elements. The sub-elements disposition is highlighted in green while the pre-cracked area is marked in red.

Figure 2: Electrode's disposition in (a) a standard coupon and in (b) a skin-strimger sub-element.

Figure 3: (a) Load-displacement and (b) R-curves of the CNT-doped and neat adhesive Mode-II joints.

Figure 4: Electromechanical behavior of the Mode-II joints showing (a) the load and (b) crack length to electrical response.

Figure 5: Electromechanical response as a function of the crack length.

Figure 6: Theoretical predictions and experimental results for (a) K=1 and (b) K=0.33

Figure 7: Schematics of the crack opening effect on Mode-I (left) and Mode-II (right) showing the differences on CNT tunneling distance (marked as red arrows).

Figure 8: Image of the fracture surface of mode-II normalized coupon showing the cohesive failure.

Figure 9: SEM images of transversal area of the CNT-doped mode-II normalized joints showing the (a), (b) thickness uniformity, (c) the globular distribution of the adhesive (highlighted in red) and (d) the adhesive interface in detail.

Figure 10: Electrical response of the skin-stringer element as a function of (a) the grip displacement and (b) the crack length.

Figure 11: Schematics of mechanical force effect on crack opening and mechanical behavior of skin-stringer element.

Figure 12: Electromechanical response of the skin-stringer element as a function of the crack length.

Figure 13: Image of the fracture surfaces of skin-stringer sub-element.

Figure 14: SEM images of the transversal section of the skin-stringer sub-element showing (a) the adhesive interface, the adhesive thickness in the (b) T and (c) web regions, the crack opening (d), (e) and bridging (f) in the joint.

TABLES

Parameter	First Stage	Second stage
Pressure	Ramp from 0 to 0.6 MPa during 15 min	0.6 MPa during 90 min
Temperature	Ramp from 25 to 175 ºC during 45 min	175 ºC during 60 min

Table 1: Cure cycle parameters of secondary bonding.

LIST OF FIGURES

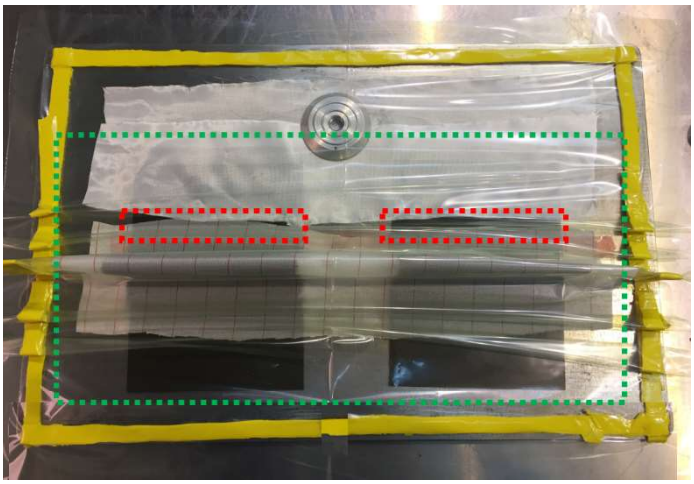

Figure 1.

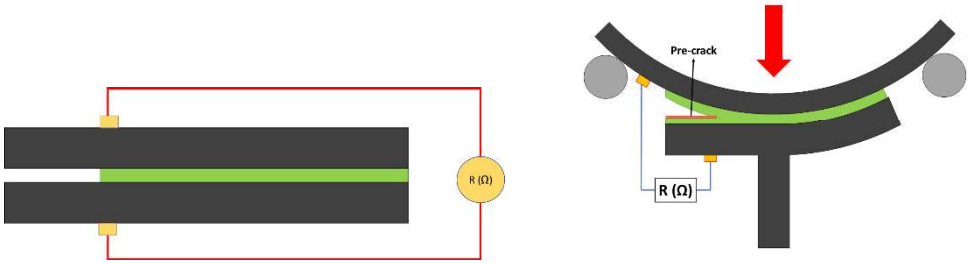

(a) (b)

Figure 2.

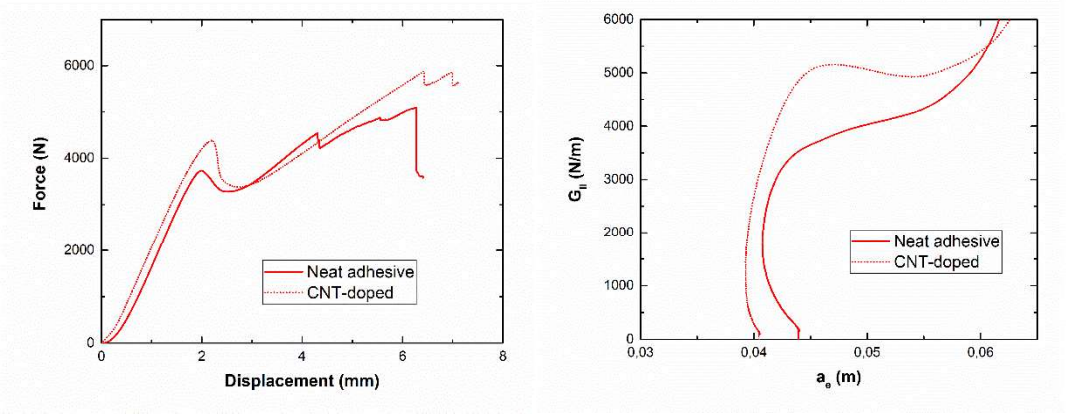

(a) (b)

Figure 3.

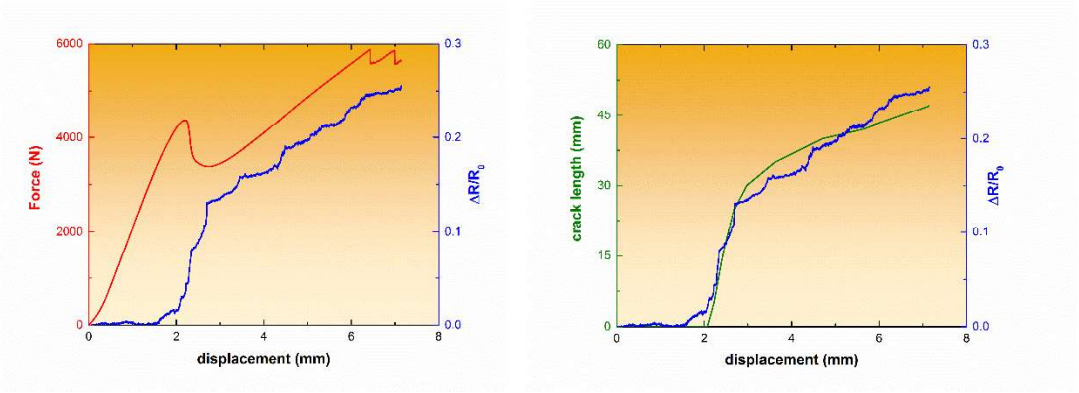

(a) (b)

Figure 4.

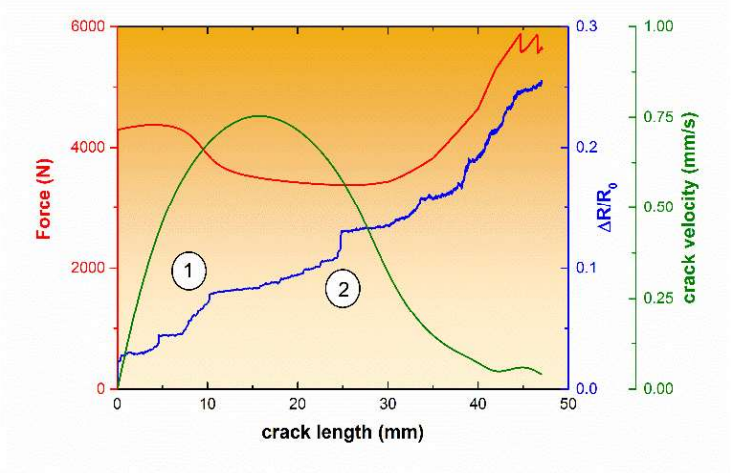

Figure 5.

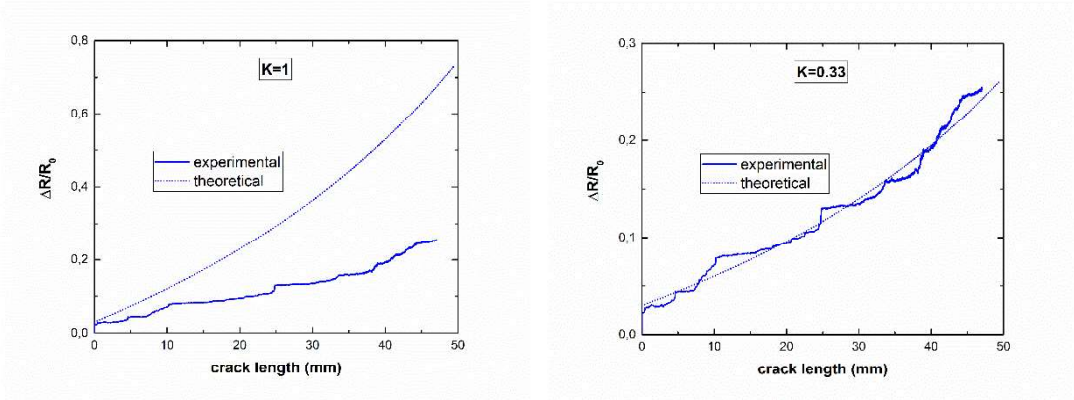

(a) (b)

Figure 6.

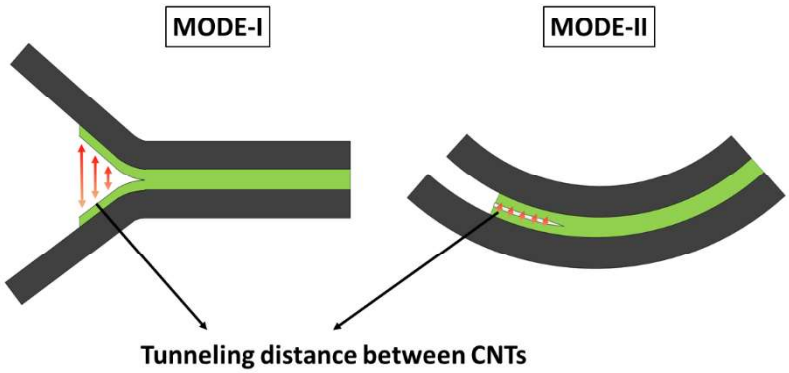

Figure 7.

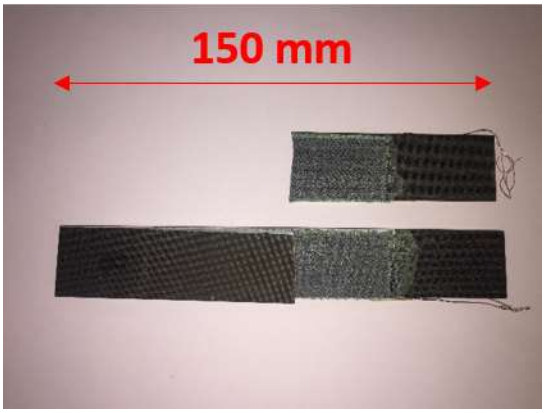

Figure 8.

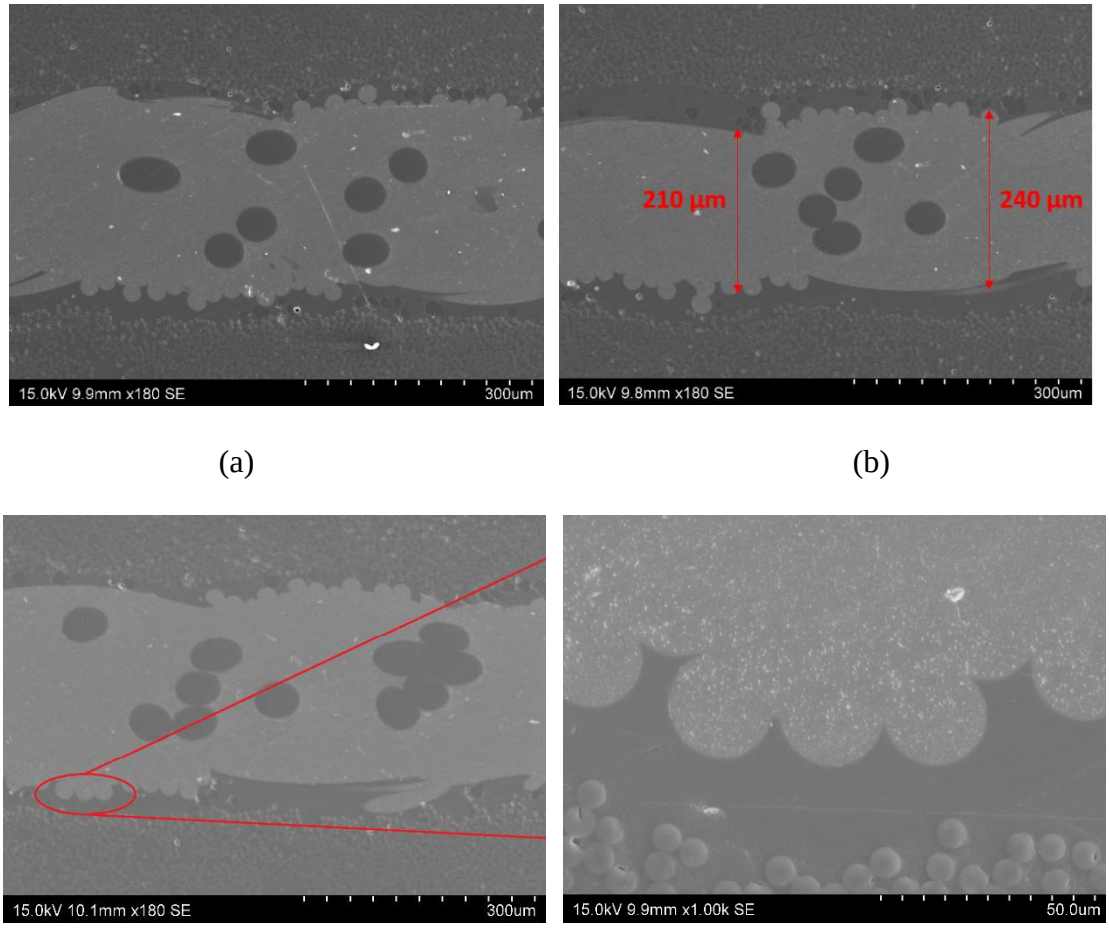

(a) (b)

(c) (d)

Figure 9.

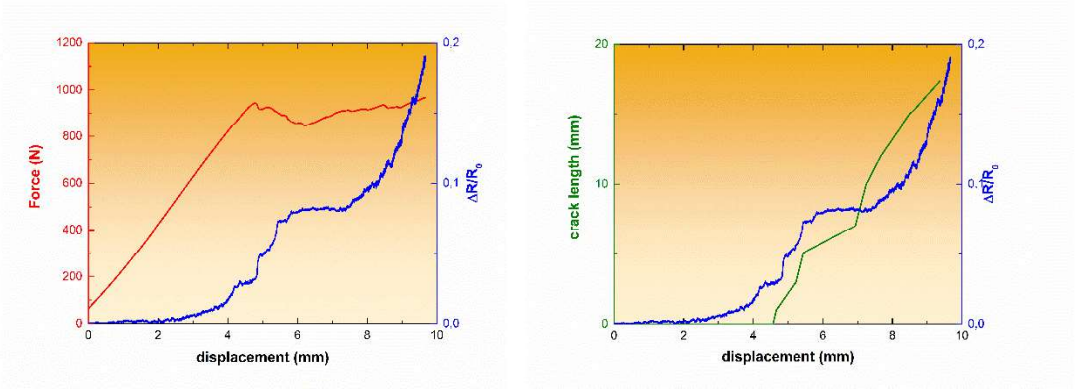

(a) (b)

Figure 10.

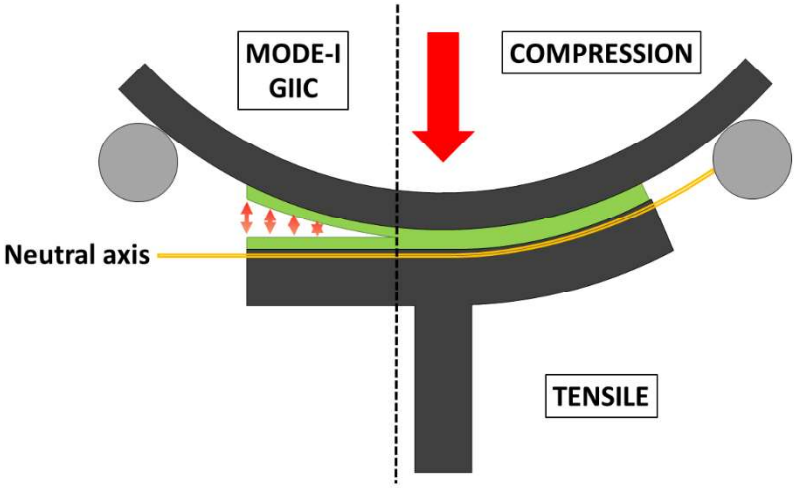

Figure 11.

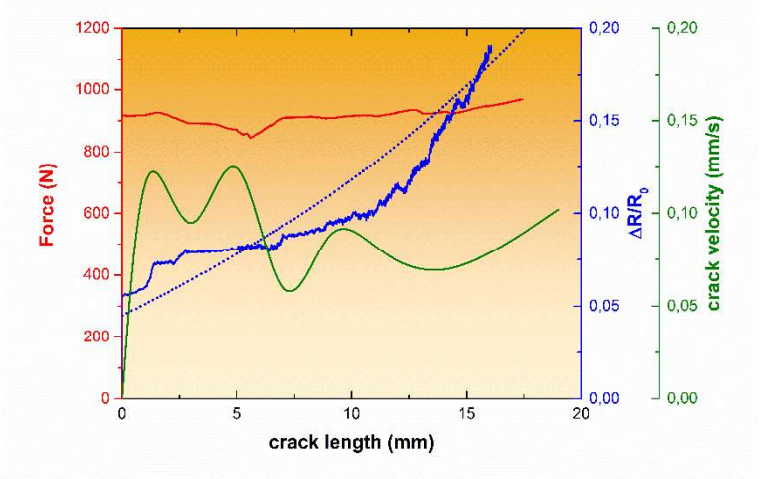

Figure 12.

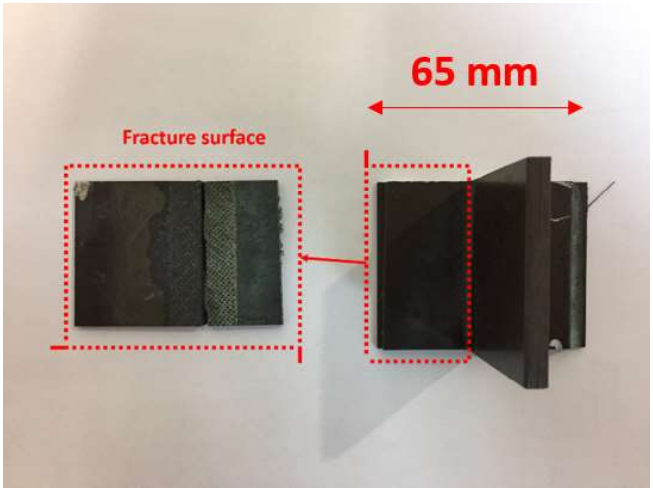

Figure 13.

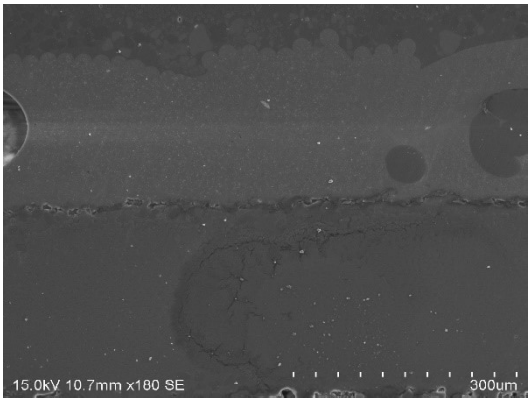

(a)

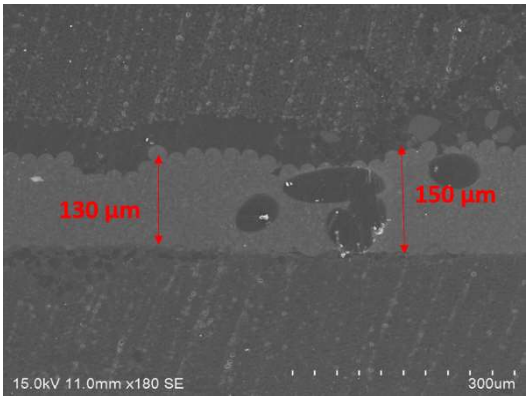

(b)

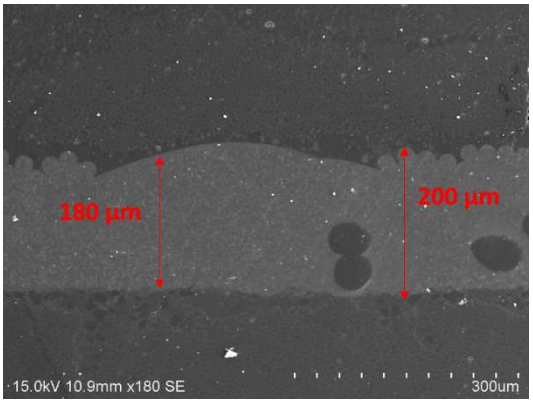

(c)

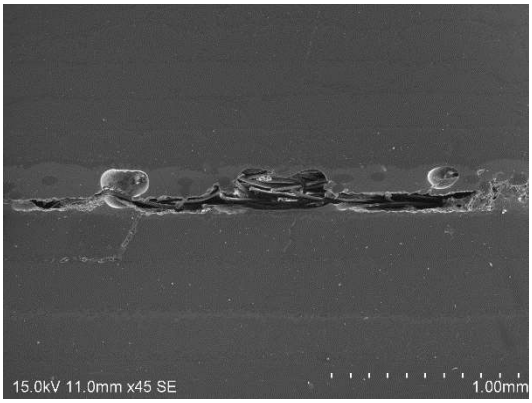

(d)

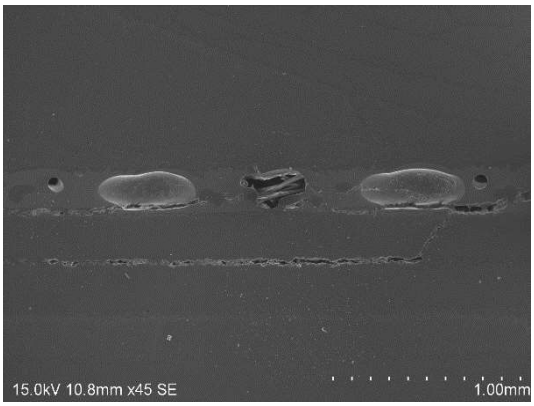

(e)

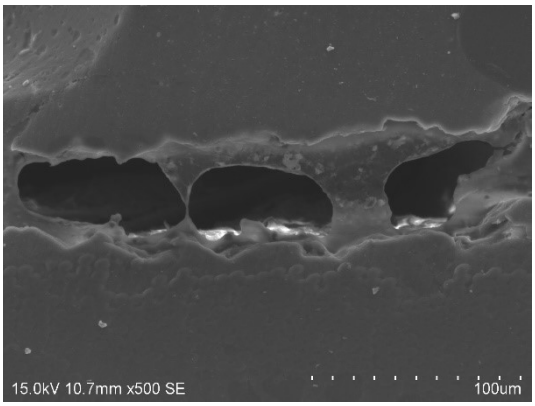

(f)

Figure 14.